Advances in Water Resources 144 (2020) 103694

Contents lists available at ScienceDirect

Advances in Water Resources

journal homepage: www.elsevier.com/locate/advwatres

Direct pore scale numerical simulation of colloid transport and retention. Part I: Fluid flow velocity, colloid size, and pore structure effects

Mandana Samari Kermani[a], Saeed Jafari[a,*], Mohammad Rahnama[a], Amir Raoof[b]

[a] Department of Mechanical Engineering, Shahid Bahonar University of Kerman, Kerman, Iran
[b] Department of Earth Sciences, Utrecht University, Utrecht, the Netherlands

ARTICLE INFO

Keywords:
Colloid transport
Agglomeration
Hydrodynamic effect
Colloid size effect
Lattice Boltzmann Method

ABSTRACT

In this study, we have developed a combined lattice Boltzmann-smoothed profile method to explore coupled mechanisms governing transport of colloids and their retention in porous media. We have considered flow in a constricted tube and included hydrodynamic, gravity, buoyancy, van der Waals and electrostatic forces to simulate colloid transport and aggregation. A major advantage of this complete formulation is that it does not require any common assumptions which neglect the effects of inter-particle forces (e.g., dilute suspension, or clean bed filtration), and pore structure changes due to colloid retention. The results show an increase in colloid aggregation and surface coverage as pore velocity decreases. However, the pore void fraction and its conductivity show a reduction with decreased velocity. In the presence of a secondary energy minimum, rolling of colloids on the grain surface is demonstrated to be the major mechanism that prevents pore clogging. Details of these observations are provided and a comprehensive sensitivity analysis of model parameters is performed and discussed.

1. Introduction

Understanding colloid transport processes is essential for predicting transport of colloidal contaminants and microorganisms such as toxic nanoparticles and viruses. Colloids may act as pollutants or may carry other contaminants deep into the subsurface (Roy et al., 2018; Bakshi et al., 2015; Gavrilescu, 2014; Sen, 2011). Several mechanisms influence colloid filtration. A major mechanism is straining which refers to colloid removal by a spectrum of physical process including size exclusion, bridging across pore spaces, or the retention of colloids in low velocity regions of porous media such as crevice sites and dead end pores. This mechanism is affected by the colloid to collector diameter, pore size distribution, van der Waals, electric double layer, and hydrodynamic forces (Torkzaban et al., 2008; Bradford et al., 2007; Bradford et al., 2006; Bradford et al., 2002). When the colloid size is larger than the pore throat size, size exclusion takes place which may completely clog the pore space (Bradford and Torkzaban, 2013; Babakhani, 2019). For smaller colloids with size comparable to the pore throat size, the bridging mechanism may occur when several particles simultaneously arrive at a throat location. This mechanism is affected by colloid concentration, hydrodynamic forces, the ratio of particle size to the throat size, the pore size distribution, and it is shown to be the mechanism responsible for permeability reduction in porous media (Ramachandran et al., 2000; Bacchin et al., 2014; Torkzaban et al., 2015). When particles are much smaller than the pore size, surface deposition is primarily influenced by adhesive forces and mass transfer of particles to the surface which occurs by interception, gravitational sedimentation, and Brownian motion (Yang and Balhoff, 2017; Yao et al., 1971).

Many studies have reported results from column experiments to understand and simulate transport and removal mechanisms of colloids, microorganisms, and nanoparticles. Results have shown that many factors influence colloid transport and retention including: solution ionic strength (IS) (Bradford and Torkzaban, 2013; Jin et al., 2017; Chen et al., 2017; French et al., 2009; Zevi et al., 2009); pH (French et al., 2009; Fujita and Kobayashi, 2016; Zhang et al., 2010); electrolyte valence and type (French et al., 2009; Zhang et al., 2010); particle and pore surface zeta potential (ζ) (Saleh et al., 2008; Dunphy Guzman et al., 2006); fluid velocity (Zhang et al., 2018; Perez et al., 2020; Bennacer et al., 2017; Zhang et al., 2015; Johnson and Tong, 2006); suspension concentration (Wang et al., 2012; Bradford et al., 2009); coating materials (Micić et al., 2017; Morales et al., 2011); colloid and grains size and shape (McNew et al., 2017; Syngouna and Chrysikopoulos, 2012; Pelley and Tufenkji, 2008); grain size distribution (Ahfir et al., 2017; Hammadi et al., 2017; Chalk et al., 2012); gravity (Chrysikopoulos and Syngouna, 2014; Kim and Whittle, 2006); surface roughness (Xinqiang et al., 2019; Henry and Minier, 2018; Bradford et al., 2017; Torkzaban and Bradford, 2016); and physical and chemical heterogeneities (Bradford et al., 2013; Li and Ma, 2019;

* Corresponding author.
E-mail address: jafari@uk.ac.ir (S. Jafari).

https://doi.org/10.1016/j.advwatres.2020.103694
Received 13 February 2020; Received in revised form 9 June 2020; Accepted 13 July 2020
Available online 15 July 2020

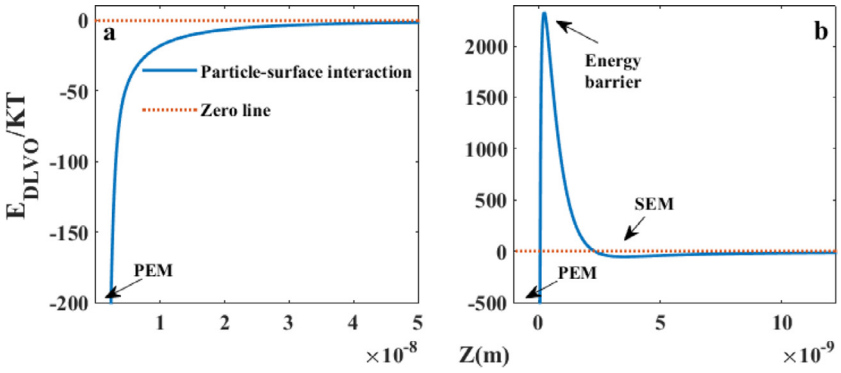

Fig. 1. DLVO interaction energy profile versus surfaces distance (particle size $d_p = 3$ μm, IS = 0.3 M, $\zeta = \pm 45.56$ mV). **(a)** A completely attractive profile between oppositely charged particles and surfaces; **(b)** A profile with SEM, PEM, and energy barrier between particles and surfaces with similar charges.

Li et al., 2017; Bradford and Torkzaban, 2013; Shen et al., 2013). Considerable amounts of retained colloids can be released by increasing the flow velocity, decreasing the solution IS, increasing the pH, when adsorbed divalent cations are exchanged for monovalent cations, after flow interruptions, and following water drainage and imbibition cycles (Bradford and Torkzaban, 2013; Torkzaban et al., 2008; Seetha et al., 2014). For example, scouring of colloids and co-existing aggregates by hydrodynamic forces can contribute significantly to release and mobilization of colloids to deeper depths (Chaumeil and Crapper, 2014; Ahfir et al., 2017). The macroscopic advection-dispersion equation with one-site or two-site kinetics is commonly used to simulate measured breakthrough curves (Katzourakis and Chrysikopoulos, 2019; Schijven et al., 2013; Simunek et al., 2005; Schijven and Hassanizadeh, 2000). However, breakthrough curves and profiles of retained colloids typically exhibit time- (e.g., plateau region increases or decreases with time) and depth-dependent (e.g., hyper-exponential or non-monotonic distributions with depth) retention behavior that can depend on physical parameters such as grain size, water content, flow rate, and chemical properties such as solution IS and pH (Torkzaban et al., 2008). A fundamental understanding and ability to predict the controlling mechanisms and factors that influence colloid transport, retention, and release is hampered by the complexity, coupling, and the number of processes that occur at the column-scale.

To overcome this challenge, several studies have employed Eulerian or Lagrangian approaches to numerically simulate colloid transport, retention, and release at the pore-scale (Seetha et al., 2014; Seetha et al., 2015; Raoof and Hassanizadeh, 2010; Raoof et al., 2010). However, the full complexity and coupling of various factors have not been considered in these works. For example, previous pore-scale simulations have made simplifying assumptions such as dilute suspension, clean bed filtration, and irreversible attachment (Seetha et al., 2014; Seetha et al., 2015; Raoof and Hassanizadeh, 2010; Raoof et al., 2010). Dilute suspensions imply that interactions among particles can be neglected. Clean bed filtration neglects the influence of attached particles on pore structure, flow streamlines, and particle transport, whereas irreversible attachment disregards particle release and remobilization. It is important to develop pore-scale simulation approaches that are not constrained by these simplifications in order to assess the validity and impact of these assumptions on colloid transport and fate.

The interaction energy between two charged surfaces is commonly calculated using theory by Derjaguin-Landau-Verwey-Overbeek (DLVO) which considers the combined effects of van der Waals and electric double layer interactions (Derjaguin and Landau, 1941; Verwey and Overbeek, 1948). The net interaction can result in conditions with an entirely attractive or a totally repulsive, or an energy profile in which a primary and a secondary minimum exist. For surfaces with opposite charges, particle deposition is favorable because both van der Waals and electric double layer interactions are attractive (Fig. 1a). In this case, a deep primary energy minimum (PEM) is formed at very close distances between the two surfaces such that attached particles do not detach from the surface (e.g., irreversible attachment). When the two surfaces are similarly charged, the electric double layer interaction is repulsive and the van der Waals interaction is attractive. An energy barrier against deposition can exist under these electrostatically unfavorable conditions. In this case, particle attachment in a PEM can only occur if the energy barrier is sufficiently small for particles to diffuse over it. However, particles may reversibly attach in a secondary energy minimum (SEM) which is developed at distances exterior to the energy barrier (Fig. 1b) (Messina et al., 2015, p. 25). Early trajectory analysis applications that have studied particle retention surfaces have been found to be unrealistic because deposited particles can continue to roll over the surface (Bai and Tien, 1997; Das et al., 1994; Sharma et al., 1992; Hubbe, 1984).

Although several valuable experimental observations and numerical models exist which include different transport and adsorption parameters, there is still a gap due to the lack of mechanistic studies that provide insights on parameters influencing colloid fate in porous media. This study aims at filling this research gap by mechanistically simulating colloid transport and retention at the pore scale. We have developed fully coupled numerical models to perform several simulations under both favorable and unfavorable conditions that explicitly included detailed physical processes with no assumptions of dilute suspensions and clean bed conditions. The effect of fluid flow on the movement of particles as well as the effect of particle motion and rotation on fluid flow was simulated by including buoyancy/gravity forces and hydrodynamic effects for both shear and normal stresses (e.g., a two-way coupling between fluid flow and particle transport equations). The interactions between particles as well as particle-surface interactions were considered and calculated using DLVO theory. The presence of aggregates was considered on deposition processes, whereas classical filtration models assume homogeneous pore space and largely ignore colloid aggregation. Moreover, retained particles that interact with the SEM can roll over the surface to the outlet, be immobilized, or detach to the bulk flow under unfavorable conditions. We consider the mentioned mechanisms and perform a large number of simulations (over 160) to explore the effects of flow velocity, colloid size, and pore structure evolution on colloid transport, retention, aggregation and release. The effects of these parameters on colloid behavior is quantified using dynamically changing particle agglomerates, particle-particle, and particle-grain surface interactions, available surface area, pore hydraulic conductivity and void fraction. Results from this study provide a clear image of mechanisms controlling colloids transport and fate in the pore space of a porous medium.

2. Methods and parameters

2.1. Lattice Boltzmann method

The developed model uses D_2Q_9 lattice Boltzmann method (LBM) to solve mass balance and momentum conservation equations for the steady-state flow of an incompressible Newtonian fluid at low Reynolds numbers. This model uses the discretized form of the Boltzmann equa-

tion with an external force term and applies the Bhatnagar-Gross-Krook (BGK) collision approximation as:

$$f_\alpha\left(\boldsymbol{x}+\boldsymbol{e_\alpha}\Delta t, t+\Delta t\right)-f_\alpha(\boldsymbol{x},t)=-\frac{1}{\tau}\left[f_\alpha(\boldsymbol{x},t)-f_\alpha^{eq}(\boldsymbol{x},t)\right]-3\omega_\alpha\rho\boldsymbol{e_\alpha}.\boldsymbol{F}/c^2 \tag{1}$$

where f_α and f_α^{eq} are the distribution and equilibrium distribution functions, respectively. The equilibrium distribution function can be written as:

$$f_\alpha^{eq}=\omega_\alpha\rho\left[1+3\frac{\boldsymbol{e_\alpha}.\boldsymbol{u}}{c^2}+\frac{9}{2}\frac{\left(\boldsymbol{e_\alpha}.\boldsymbol{u}\right)^2}{c^4}-\frac{3}{2}\frac{\boldsymbol{u}.\boldsymbol{u}}{c^2}\right] \tag{2}$$

where c, $\boldsymbol{x}$, and t are lattice speed, lattice coordinate and time, respectively. The weight coefficients, ω_α, and the discrete velocity vectors, $\boldsymbol{e_\alpha}$, in each of the nine α directions in the D2Q9 model are described as:

$$\boldsymbol{e_\alpha}=\begin{cases}(0,0) & \alpha=0\\ (1,0),(0,1),(-1,0),(0,-1) & \alpha=1,2,3,4\\ (1,1),(-1,1),(-1,-1),(1,-1) & \alpha=5,6,7,8\end{cases} \tag{3}$$

$$\omega_\alpha=\begin{cases}4/9 & \alpha=0\\ 1/9 & \alpha=1,2,3,4\\ 1/36 & \alpha=5,6,7,8\end{cases} \tag{4}$$

The dimensionless relaxation time, τ, is defined as $\tau=\nu/c_s^2\Delta t+0.5$. τ controls the relaxation time-scale of the viscous stress in the numerical formulation which in its physical representation relates to the fluid kinematic viscosity, ν, and the speed of sound in the lattice (defined as $c_s^2=c^2/3$). $\boldsymbol{F}$ considers the external body forces exerted on the fluid which in this study simulates the effect of particles on fluid flow. In the discretized velocity space, the macroscopic fluid density, ρ, and velocity, $\boldsymbol{u}$, can be defined as:

$$\rho(\boldsymbol{x},t)=\sum_{\alpha=0}^{8}f_\alpha(\boldsymbol{x},t) \tag{5}$$

$$\rho(\boldsymbol{x},t)\,\boldsymbol{u}(\boldsymbol{x},t)=\sum_{\alpha=0}^{8}\boldsymbol{e_\alpha}f_\alpha(\boldsymbol{x},t) \tag{6}$$

By using the Chapman-Enskog procedure, the incompressible Navier-Stokes equations can be obtained from Eq. (1). Details of the LBM and derivation of Navier-Stokes equations can be found in Luo (1993), Succi (2001), Guo and Shu (2013).

2.2. Smoothed profile method

In the developed model, we have applied a Smoothed Profile Method (SPM) to represent the individual particles. The SPM represents the solid particles using a profile function (ϕ) which is equal to one within the particle and approaches zero within the fluid phase. We have considered round particles and Eq. (7) provides the profile which uses the particle radius (R_P), the center position of the particle ($\boldsymbol{R}_P$), and the interface thickness (ξ) to provide the domain occupied by a given particle p:

$$\varphi_P(\boldsymbol{x},t)=s\left(R_P-\left|\boldsymbol{x}-\boldsymbol{R}_P(t)\right|\right)$$
$$s\left(L_P\right)=\begin{cases}0 & L_P<-\xi/2\\ \frac{1}{2}\left(sin\left(\frac{\pi L_P}{\xi}\right)+1\right) & \left|L_P\right|\le\xi/2\\ 1 & L_P>\xi/2\end{cases} \tag{7}$$

The calculated total profile function, $\varphi(\boldsymbol{x},t)=\sum_{P=1}^{N_P}\varphi_P(\boldsymbol{x},t)$, is used to determine particle regions based on all N particles present within the pore space. Afterwards, the particles velocity

$$\varphi(\boldsymbol{x},t)\,\boldsymbol{u_P}(\boldsymbol{x},t)=\sum_{P=1}^{N_P}\varphi_P(\boldsymbol{x},t)\left[\boldsymbol{U}_{C_p}(t)+\boldsymbol{\omega}_P\times\left\{\boldsymbol{x}-\boldsymbol{R}_P(t)\right\}\right] \tag{8}$$

at time t and position $\boldsymbol{x}$, $\boldsymbol{u_P}(\boldsymbol{x},t)$, is calculated by assuming rigid motion of particles as: where $\boldsymbol{U}_{C_p}$ and $\boldsymbol{\omega}_P$ are the translational and the angular velocities of particles, respectively. In this study, particles dynamically flow through the fluid-filled pore space. We apply f_H function to obtain the fluid-solid interaction forces and add this function to the LBM formula (i.e., in form of a body force $\boldsymbol{F}$ in Eq. (1)). The f_H function is written as:

$$f_H=-\varphi(\boldsymbol{x},t)f_P(\boldsymbol{x},t)=-\varphi(\boldsymbol{x},t)\left(\boldsymbol{u_P}(\boldsymbol{x},t)-\boldsymbol{u}(\boldsymbol{x},t)\right) \tag{9}$$

where $\boldsymbol{u}(\boldsymbol{x}, t)$ is the fluid velocity at time t and position $\boldsymbol{x}$, and ϕf_P represents the fluid-solid interaction forces acting on the solid phases. The momentum conservation law can be used to obtain the integrated hydrodynamic force, F_P^H, and torque, T_P^H, exerted on each individual solid particle as:

$$F_P^H=\int_{\forall_p}\rho\varphi(\boldsymbol{x},t)\left(\boldsymbol{u}(\boldsymbol{x},t)-\boldsymbol{u}_p(\boldsymbol{x},t)\right)\,d\forall_p \tag{10}$$

$$T_P^H=\int_{\forall_p}\left(\boldsymbol{x}-\boldsymbol{R}_P\right)\times\rho\varphi(\boldsymbol{x},t)\left(\boldsymbol{u}(\boldsymbol{x},t)-\boldsymbol{u}_p(\boldsymbol{x},t)\right)\,d\forall_p \tag{11}$$

Details of the SPM can be found in Jafari et al. (2011), Nakayama and Yamamoto (2005).

2.3. Equations of motion and force components for particles

To calculate a particle's translational velocity ($\boldsymbol{U}_{C_p}$) and position ($\boldsymbol{R}_P$), we have included hydrodynamic (F^H), gravitational (F^G), particle-surface ($\boldsymbol{F}_{P-S}^{EDL}$, $\boldsymbol{F}_{P-S}^{vdW}$), and particle-particle ($\boldsymbol{F}_{P-P}^{EDL}$, $\boldsymbol{F}_{P-P}^{vdW}$) forces in Eq. (17) (Chaumeil and Crapper, 2014; Derjaguin and Landau, 1941; Verwey and Overbeek, 1948; Hogg et al., 1966). The angular velocity of a particle ($\boldsymbol{\omega}_p$) is updated using Eq. (18) in which T_p is the total external torque exerted on a particle and $I_p$is the particle moment of inertia. For particle sizes considered in this study (i.e., 1, 3, and 10 μm), particle diffusion is negligible, and it is not considered in transport equations. Table 1 provides a summary of equations employed in this study. We have calculated the particle-surface interactions assuming a sphere-plate geometry and assumed that the curved pore surface is microscopically smooth (i.e., while the surface is curved there is no roughness on the surface) initially. Particle and pore surfaces are chemically homogeneous and uniformly charged. We should note that these conditions are the initial settings and during simulations, retention of particles (with different sizes and charges) on the pore surface alters the homogeneity of the pore.

A large number of simulations for colloid transport were performed for various solution IS, pore and particle surface zeta potentials (ζ), particles sizes (d_p), and average fluid velocities (U). To obtain systematic results, we have chosen a set of three values for each of these parameters presented in Table 1. Average fluid velocities (U) are related to steady-state flows before particles were injected. The fluid velocity field ($\boldsymbol{u}$) was dynamically calculated (i.e., in each time step) after particles entered the pore space using coupled formulas for fluid flow and particle motion. This allowed the effects of fluid hydrodynamic forces on particle movement and the effect of particles on fluid flow to be captured with local velocity variations. The selected range of parameters resulted in 162 different simulations to cover a range of favorable and unfavorable conditions. Several simulations were run simultaneously on a workstation PC with 32 cores and 128 GB memory. This approach was found to be more time efficient than running each simulation on multiple cores. The computational time for each simulation was, on average, around nineteen days after which a new set of simulations was run until all 162 simulations were completed. In describing results of the simulations, unless otherwise stated, particles were retained in the SEM zone of other particles to form agglomerates (which are shown by orange-color particles in figures) or in the SEM zone of the grain surface under unfavorable conditions (which are indicated by red-color particles in figures). Strong particle attachment in PEM takes place when there is no energy barrier

Table 1
This table includes the list of different forces acting on particles, equations of motion, and the considered range of parameters selected for simulations in this study.

Gravitational and DLVO forces			
Gravitational forces		$\boldsymbol{F}_P^G = \rho_P V_P g(1 - \frac{\rho}{\rho_P})$	Eq. (12)
Electrostatic force between particles and surfaces		$\boldsymbol{F}_{P-S}^{EDL} = 4\pi\varepsilon_0\varepsilon_r\zeta_P\zeta_S\kappa R_P(\frac{\exp(-\kappa h)}{1+\exp(-\kappa h)} - \frac{(\zeta_P-\zeta_S)^2}{2\zeta_P\zeta_S}\frac{\exp(-2\kappa h)}{1-\exp(-2\kappa h)})$	
		$\kappa R_P > 5$	Eq. (13)
van der Waals force between particles and surfaces		$\boldsymbol{F}_{P-S}^{vdW} = \frac{H_a R_P}{6h^2}$	Eq. (14)
Electrostatic force between two particles		$\boldsymbol{F}_{P_i-P_j}^{EDL} = 32\pi\varepsilon_0\varepsilon_r\kappa R_P(\frac{K_BT}{Ze})^2 tanh(\frac{Ze\zeta_i}{4KT})\tanh(\frac{Ze\zeta_j}{4KT})\exp(-\kappa h)$	
		$\kappa R_P > 5$	Eq. (15)
van der Waals force between two particles		$\boldsymbol{F}_{P_i-P_j}^{vdW} = \frac{32}{3}H_a D_{P_i-P_j}\frac{R_{P_i}^3 R_{P_j}^3}{(((D_{P_i-P_j}+R_{P_i})^2-R_{P_j}^2)((D_{P_i-P_j}-R_{P_j})^2-R_{P_i}^2))^2}$	Eq. (16)
Particles equations of motion			
New translational velocity		$M_P\frac{d\boldsymbol{U}_{C_P}}{dt} = \boldsymbol{F}_P^H + \boldsymbol{F}_P^G + \boldsymbol{F}_{P-P}^{DLVO} + \boldsymbol{F}_{P-S}^{DLVO}$	Eq. (17)
New angular velocity		$\boldsymbol{I}_P.\dot{\boldsymbol{\omega}}_P = \boldsymbol{T}_P$	Eq. (18)
New position of particles		$\frac{d\boldsymbol{R}_P}{dt} = \boldsymbol{U}_{C_P}$	Eq. (19)
Values of different parameters used in the simulations			
Particle diameters, dp [μm]	{3, 5, 10}	Solution Ionic strength, I.S. [M]	{0.001, 0.05, 0.3}
Mean fluid velocity, U [m/day]	{1, 5, 10}	Particles and pore surface zeta potential, ζ [mV]	{ ± 17.5, ± 45.56, ± 60}

under favorable conditions (which are shown by white-color particles in figures).

$\rho_P = 1055$ [Kg/m^3], M_P [Kg], and V_P [m^3] are density, mass, and volume of particles, respectively. $K_B = 1.38 \times 10^{-23}$ [J/K] is the Boltzmann constant, $T = 298$ [K] is temperature, $e = 1.6 \times 10^{-19}$ [C] is electron charge, $\varepsilon_0 = 8.85 \times 10^{-12}$ [C^2/Jm] is vacuum dielectric permittivity, $\varepsilon_r = 78.54$ is dielectric constant of the media, $H_a = 1.5 \times 10^{-21}$ [J] is the Hamaker constant, D_{ij} [m] is the center to center distance between two particles, h [m] is the separation distance, Z is the valence of each ion species in the electrolyte, and $\kappa = (2 \times 10^3 N_A e^2 IS/\varepsilon_0\varepsilon_r K_B T)^{1/2}$ [m^{-1}] is the reciprocal Debye length for a monovalent electrolyte where $N_A = 6.02 \times 10^{23}$ is Avogadro's number.

2.4. Torque analysis

To calculate the torque, when particles enter into the SEM of the grain surface a contact area with a lever arm of $I_x = (F_r d_P/8K)^{1/3}$ was calculated, where F_r is the sum of forces providing torques to prevent rolling (Johnson et al., 1971), and K is the composite Young's modulus for which a value of 4.014×10^9 Nm^{-2} was chosen in this study. We calculate torques at the two ends of the contact area (which is represented by a line in 2D simulations) to determine whether the trapped particles can roll forward, backward or they remain immobile on the sinusoidal pore surface (Torkzaban et al., 2007).

When a particle is moving in the bulk flow its rotation is around its center; however, when it is retained within the grain SEM, it begins rolling around the edge of its contact line. Pore-scale simulations have shown that the secondary minimum plays an important role in retention of both small and large size colloids in the absence of diffusion (i.e., for particle sizes larger than 1 μm). The contribution of SEM in particle retention increases when the interaction energy barrier increases and favorability for attachment in the PEM of the surface is reduced (Seetha et al., 2014). For much smaller particles that diffusion is a major transport mechanism, the SEM retention role is reduced and diffusive release of particles may occur.

3. Geometry and boundary conditions

In this study, we have considered a sinusoidal pore with a length of 200 μm, and an opening of 50 μm at the inlet and outlet which is reduced to 20 μm in the middle of the pore. This pore structure represents a typical pore present in glass beads or sand packs between pairs of rounded grains. The chosen pore size falls in the range of medium-sand packs, and is within the common range of pore size distributions for sandstone and carbonate rocks. The importance of the sinusoidal shape is that it captures the presence of diverging and converging velocities and streamlines in porous media. A curve boundary bounce back method was applied to simulate the pore surfaces (Bouzidi et al., 2001). At the pore inlet boundary, a parabolic velocity profile was implemented, and a constant pressure was assigned at the pore outlet. These conditions were chosen to obtain a mean steady-state flow velocity along the pore equal to 1, 5, and 10 m/d before injection of any particles. The particle injection height was selected to allow particles to enter randomly along the pore inlet face to resemble colloid trajectories in porous media. The rate of colloid injection was continued and chosen such that the surface area of entering colloids would be equal to 1188 μm^2 per injected fluid pore volume (shown by PV in the text and figures). For example, the particle injection rates were equal to 168, 60, and 15 particles per injected fluid PV in simulations using 3, 5, and 10 μm particles, respectively, when the bulk velocity was 10 m/d. These rates were equal to 2×10^8, 9×10^8, and 27×10^8 particles per milliliter of injected fluid, respectively. This approach allowed us to provide a well-defined basis for comparison of results from different simulations. The initial velocity of particles at the inlet was chosen to be equal to the fluid velocity at that location. The constructed numerical grid included 400 × 100 cells in each principal direction. We chose to only simulate 2D geometries because of the considerable computational time that was required to solve the coupled equations.

4. Results and discussion

4.1. Hydrodynamic effect

The flowing water creates a hydrodynamic force on moving and attached colloids. Our results have shown that lower velocities generate forces which are relatively weak and may not be able to overcome adhesive forces even for particles retained within the SEM zone of other particles or the pore surface. Therefore, pore clogging was more frequent in these simulations due to lower velocity values. As all the colloids are similarly charged, the condition for aggregation is unfavorable and due to colloid-colloid SEM interactions. However, the retention of colloids on the grain surface can occur within the SEM zone under unfavorable conditions, or within the PEM zone under favorable conditions. Once colloids are attached on the pore surface under favorable conditions, then condition may reverse from favorable to unfavorable and SEM interactions between approaching and already-attached colloids may result in multilayer deposition.

Fig. 2a and b examine the attachment and clogging behavior of 5 and 3 μm sized particles at several velocities under favorable conditions when an intermediate IS of 0.05 M was considered. Pore clogging was

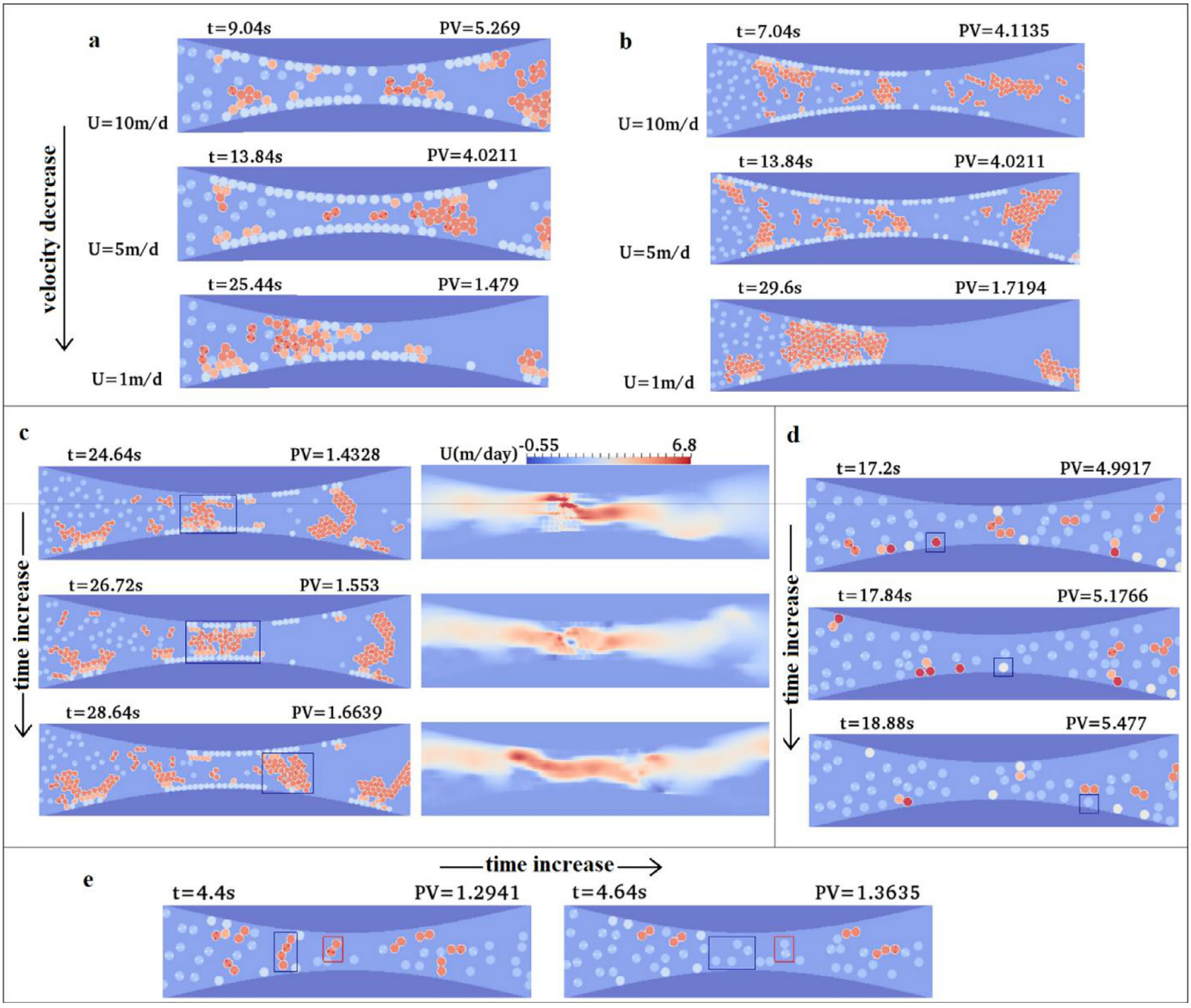

Fig. 2. Hydrodynamic effects on particles transport. (a, b) Pore clogging only takes place under the lowest fluid velocity of 1 m/d under favorable conditions. **(a)** dp = 5 μm, IS = 0.05 M, ζ = 60 mV, and **(b)** dp = 3 μm, IS = 0.05 M, ζ = 17.5 mV. **(c)** Hydrodynamic shear forces pushes agglomerates through the pore throat which causes significant variations in the local velocity (dp = 3 μm, IS = 0.05 M, ζ = 45.56 mV, U = 1 m/d, favorable conditions). **(d)** Hydrodynamic forces detach and remobilize the SEM-retained particles from the grain surface under unfavorable conditions. Rectangle markers are used to show particle remobilization (dp = 5 μm, IS = 0.001 M, ζ = 17.5 mV, U = 5 m/d). **(e)** The increased hydrodynamic force generated in the pore throat ruptures agglomerate clusters and releases colloids which can easily pass through the pore throat (d_p = 5 μm, IS = 0.001 M, ζ = 45.56 mV, U = 5 m/d, favorable conditions).

observed at a fluid velocity of 1 m/d for 5 μm particles when ζ = 17.5, 45.56, and 60 mV and for 3 μm particles when ζ = 17.5 mV. Conversely, colloids formed a single attached layer on the grain surface that delayed pore clogging when higher velocities of 5 and 10 m/d were applied; e.g., colloids did not form multi-layers that were needed to clog the pore.

Approaching particles moving in the bulk solution can generally attach within the SEM zone of deposited particles and form multilayer deposition. During this process, the pore size available to flow decreases, and generates larger shear forces which are more effective in mobilizing particles and agglomerates. The increased shear forces therefore hamper strong pore clogging. This effect is shown in Fig. 2c where the increased shear force resulted in separation of retained particles and remobilization of aggregates. The non-uniform shape of the pore generates hydrodynamic forces which are stronger at the location of the pore throat and can remobilize retained particles. We describe this effect using Fig. 2d. This figure shows a particle (the red particle in the blue box) which is rolling over the surface to reach the pore constriction. The increased shear force detaches this particle from the grain surface and makes it rotate around its own center while still experiencing DLVO interactions with the surface (shown as the white particle in the blue box). Ultimately, this particle is completely released from the surface and enters the bulk flow (shown as the light blue particle in the blue box).

The velocity field may change due to particle retention and pore shape, and this can deform clusters of aggregated colloids. The generated velocities may break a cluster of aggregated colloids into smaller groups depending on the relative strength of the shear force to the depth of the SEM. In Fig. 2e, two agglomerates are shown in blue and red boxes. Each aggregate remains intact until passing through the throat, but then they disaggregate due to increased fluid velocity and shear force that can overcome weak SEM interactions among these particles at low IS of 0.001 M.

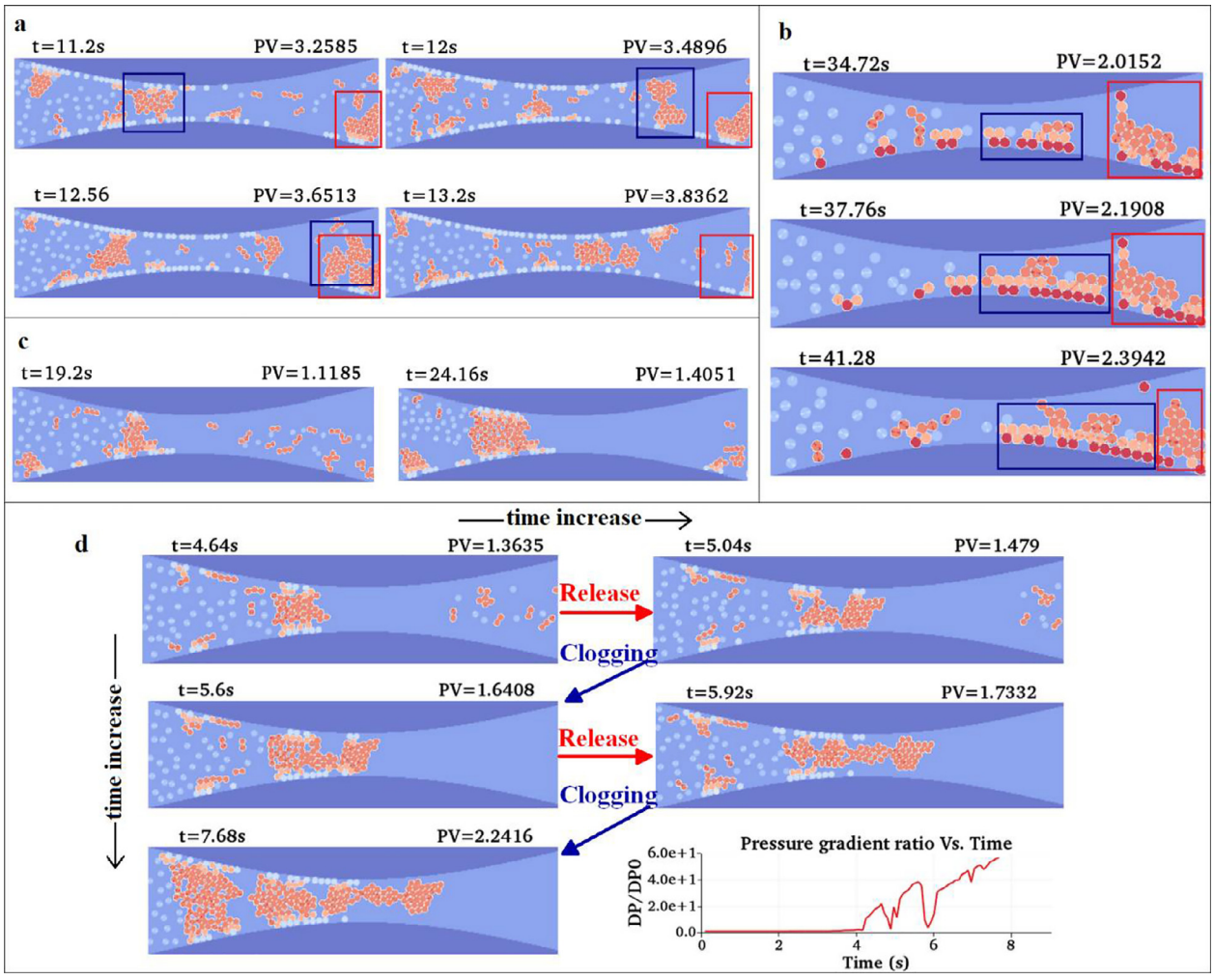

Fig. 3. Colloid remobilization and clogging. (a, b) Mobile agglomerates can collide with stagnant agglomerates and remobilize them **(a)** d_p = 3 μm, IS = 0.05 M, ζ = 17.5 mV, U = 5 m/d, favorable conditions. **(b)** d_p = 5 μm, IS = 0.3 M, ζ = 60 mV, U = 1 m/d, unfavorable conditions. **(c)** When hydrodynamic force is not sufficiently large, colloids approaching the pore throat will accumulate and ultimately clog the pore (d_p = 3 μm, IS = 0.3 M, ζ = 45.56 mV, U = 1 m/d, favorable conditions). **(d)** Dynamic remobilization and clogging events create considerable fluctuations in local velocity field and pressure gradient which cause changes in the hydrodynamic force acting on colloids (d_p = 3 μm, IS = 0.3 M, ζ = 45.56 mV, U = 5 m/d, favorable conditions).

The velocity field begins to diverge after passing the pore throat and hydrodynamic forces decrease. Particles and agglomerates become less mobile due to this decrease in force. In this situation, approaching mobile colloids and aggregates with higher velocities can collide with less mobile agglomerates after passing through the narrow pore throat. The outcome of this collision depends on the acquired momentum of the aggregate and it may begin to move faster. Fig. 3a-b show that agglomerates become less mobile after passing through the throat location (marked by red boxes in figures) and then they start to move faster once approaching mobile colloids (marked by blue boxes) collide with them.

The coupling between fluid flow and colloid transport generates transient changes in the velocity field. In particular, clogging builds up fluid pressure and increases fluid velocity among agglomerated particles to maintain the fluid flow prescribed by the inlet boundary condition. If the generated force is not large enough to break the cluster and remobilize retained particles, agglomerates begin to clog the pore as shown in Fig. 3c. However, if the increase in shear flow is enough to break up the agglomerates, the free pore space recovers and remobilization relaxes the pressure field and lowers the fluid velocity. Fig. 3d shows examples of pressure gradient fluctuations caused by pore clogging and subsequent rupture of agglomerates. Similar observations were made by Dunphy Guzman et al. (2006). They found that shear forces increased within narrow channels when nanoparticles started to clog, but that aggregates can break apart and reform.

In this section we provided some physical insights in how particles interact with each other and the pore surface at the pore scale. The effect of these interactions on particle agglomeration, pore surface coverage, conductivity and void fraction is discussed in Sections 4.1.1 and 4.1.2 under favorable and unfavorable conditions, respectively.

4.1.1. Effects of velocity on colloid transport and change of pore properties: favorable conditions

In this section we will explore how flow velocity influences colloid transport, agglomeration, grain surface coverage, pore conductivity, and pore void fraction. The size and stability of an aggregate is influenced by flow velocity. We define particle coordination number to describe the connectivity of colloid members within an aggregate. The particle coordination number for any colloid is the number of particles that are attached to that colloid. The average coordination number was calculated from this information for each aggregate and for the whole pore. The normalized grain surface coverage was calculated as the ratio of occupied grain surface area by deposited particles to the total grain surface. In this study, grain surface area that was occupied by a retained colloid was calculated by projecting the colloid diameter on the grain surface.

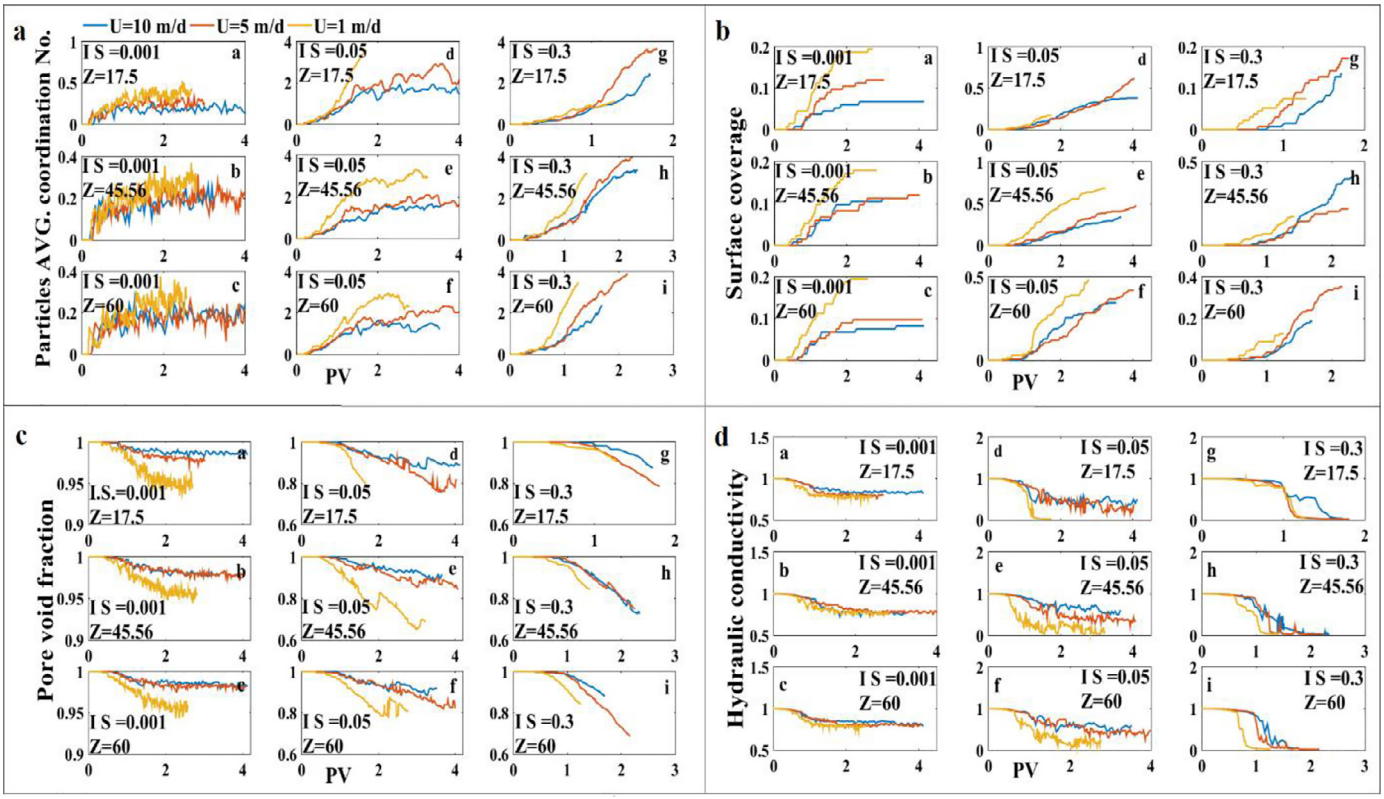

Fig. 4. Change of aggregates connectivity, grain surface coverage, pore void fraction, and hydraulic conductivity under favorable conditions. Change of average particle coordination number **(a)**, pore surface coverage **(b)**, pore void fraction **(c)**, and pore conductivity **(d)** with injected pore volume at different fluid velocities and IS (d_p = 3 μm). Z [mV] denotes the zeta potential and IS [M] the solution ionic strength.

Our results show that the average coordination number (i.e., connectivity among colloid members of aggregates) decreases as the flow velocity and hydrodynamic force increases because aggregates are ruptured into smaller clusters (Fig. 4a). The generated clusters can often flow deeper into the pore space due to their smaller size and this influences the arrangement of the retained colloids on the grain surface. The increased hydrodynamic force lowers the grain surface coverage (Fig. 4b) and increases the void fraction and conductivity of the pore (Fig. 4c-d). These observations agree with findings from Li et al. (2017).

Column experiments in Ko and Elimelech (2000) showed that larger flow velocities create a greater distance between attached particles. This space is called the shadow zone, and colloids do not deposit within this space (Ko and Elimelech, 2000). As flow velocity decreases, shadow zones grow smaller and their effect on retention of other particles and change of grain surface coverage becomes negligible. Our simulations showed the same general trend in grain surface coverage. However, slight deviations from this trend are probable because interactions between colloids and fluid flow are complex and dynamic. For example, in Fig. 4b (plots f and h) the simulations with flow velocity of 10 m/d showed a higher surface coverage than the simulations with a lower velocity of 5 m/d. For the simulation shown in Fig. 4b (f) with a velocity of 5 m/d, we observed that an agglomerate near the inlet changed the flow field such that fewer particles were carried towards the grain surface and attached. In this case, the grain surface coverage was lower at velocity of 5 m/d than 10 m/d until the aggregate started to move and the relaxed fluid flow allowed more attachment.

Fig. 4b (h) shows that the pore space was clogged for all three velocities when the IS was 0.3 M. However, several remobilization events happened for the 3 μm agglomerates before complete pore clogging. Remobilization happened when an increase in the velocity to 10 m/d made more particles detach and move further along the pore space. This increased velocity ruptured aggregates into individual or small-size clusters which deposit on the grain surface in a single layer pattern and increase the surface coverage compared to a lower velocity of 5 m/d.

When particle size was increased from 3 to 5 μm, the observed surface coverage for most combinations of parameters was lower for U = 10 m/d compared to U = 5 m/d. The exceptions to this trend were the simulations with IS = 0.3 M for which pore clogging took place close to the pore inlet before the grain surface could contact many colloids. Therefore, for larger particles, fast clogging close to the pore inlet and blockage of flow through the pore can prevent an increase in the grain surface coverage for the whole pore. The 5, and 10 μm particles showed less remobilization events in comparison to 3 μm particles mainly because they formed stronger attractive particle-particle forces. These results agree with findings of Ahfir et al. (2017) who showed that under lower flow velocities the hydrodynamic forces were not sufficient to prevent deposition or to mobilize attached particles (Ahfir et al., 2017). According to their study, while attachment happened to colloids of different sizes, larger colloids attached mainly close to the inlet of the sample. However, larger particles could travel further when the flow velocity was increased and this resulted in a smoother profile of adsorbed mass along the sample (Ahfir et al., 2017).

4.1.2. Effects of velocity on colloid transport and change of pore properties: unfavorable conditions

The connectivity among the aggregated colloids under unfavorable condition is shown in Fig. 5a for 3 μm colloids. Simulations using the lower velocity of U = 1 m/d provided the highest particle coordination number. The particle coordination number shows more fluctuations under low IS (0.001 M) because retention and remobilization take place several times. The coordination number becomes larger at a higher IS because of a deeper SEM. In comparison with favorable conditions, the coordination numbers under flow velocities of 5 and 10 m/d have closer values to the coordination numbers related to velocity of 1 m/d under

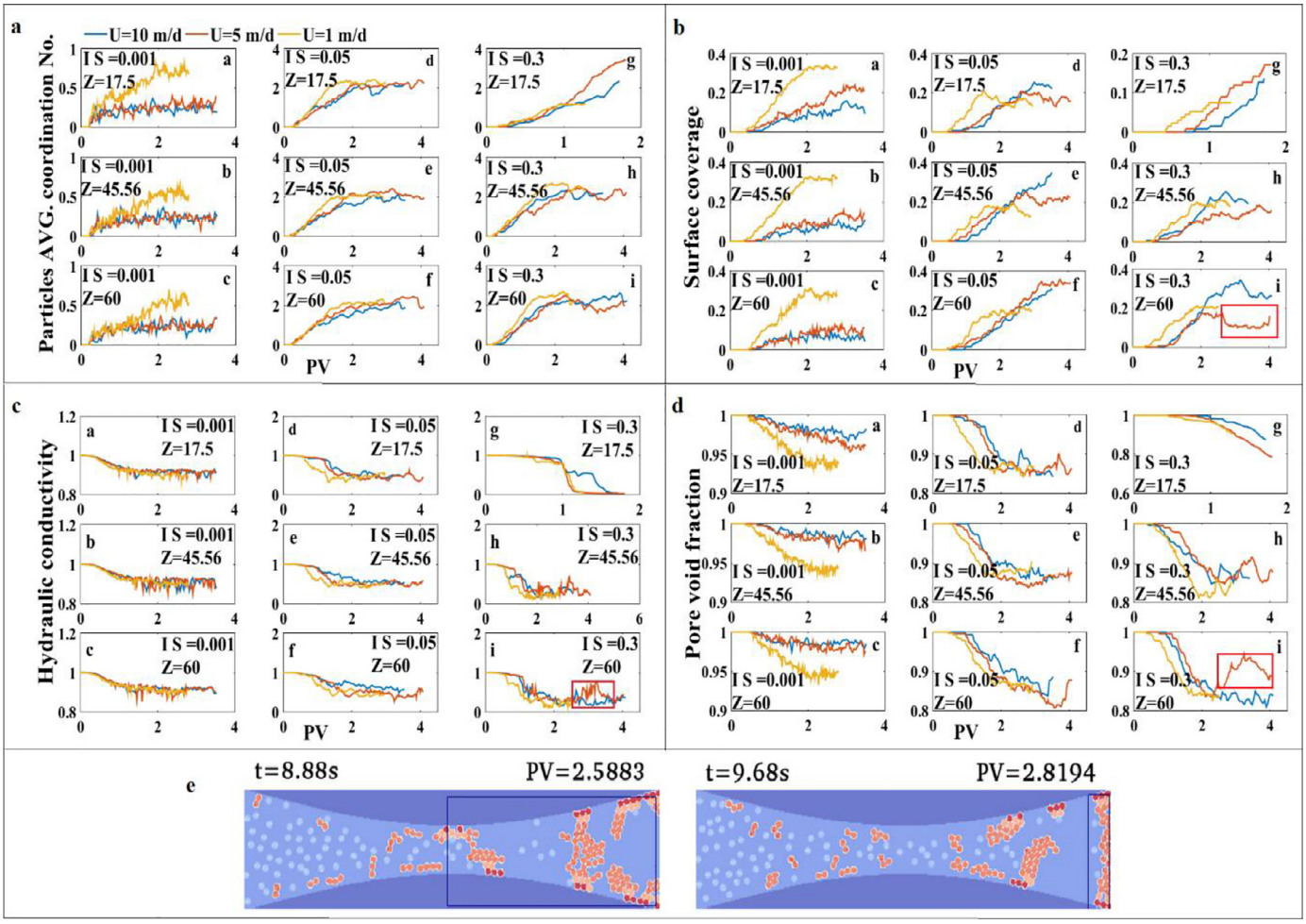

Fig. 5. Change of aggregate connectivity, grain surface coverage, hydraulic conductivity, and pore void fraction under unfavorable condition. Change of average particle coordination number **(a)**, pore surface coverage **(b)**, pore conductivity **(c)**, and pore void fraction **(d)** with injected pore volume at different fluid velocities (d_p = 3 μm). **(e)** Pore conductivity and void fraction fluctuations due to leaving of a large agglomerate out of the pore (d_p = 3 μm, IS = 0.3 M, ζ = 60 mV, U = 5 m/d, unfavorable conditions). Z [mV] denotes the zeta potential and IS [M] the solution ionic strength.

unfavorable conditions. This is because under this condition, the second layer of retained particles in SEM distance of the surface rolling particles can remain connected to them while these particles are rolling on the pore surface. However, under favorable conditions, the first layer of particles is strongly attached to the surface, and the second layer particles in their SEM distance have to be separated from them to continue their path toward the outlet.

An important transport mechanism under unfavorable condition is the rolling of retained particles over the surface which enables them to move forward without detaching from the surface. Particles and agglomerates move faster when the applied velocity and hydrodynamic force increases. They can collide and form new aggregates with larger coordination numbers during movement. While simulations using 3 and 5 μm particles showed similar behaviors, 10 μm particles showed larger fluctuations because hydrodynamic forces and SEM interactions with the grain surface and other particles were stronger.

Surface coverage is highly affected by the formation of agglomerates. When conditions are not favorable for creation of large agglomerates, transport happens in the form of individual colloids or small agglomerates which can deposit on grain surfaces, especially at lower flow velocities. This occurred under low IS = 0.001 M condition, and when the IS = 0.05 M for fluid injection of less than 2 PV or high values of zeta potential (about 60 mV) because the surface coverage increased as the flow velocity decreased (Fig. 5b, plots (a, b, c, f, and d (PV)<2, e (PV<2)). Fig. 5b also shows that for moderate to high IS values (0.05 and 0.3 M) the surface coverage raised considerably when the velocity increased from 5 to 10 m/d (Fig. 5b, plots (d, e, h, i) (PV>2)). In contrast, surface coverage was higher for lower flow velocities under favorable conditions due to the reduction of the shadow zones behind strongly attached particles. Under unfavorable conditions, the shadow zone can change as particles roll over the grain surface and the distance among rolling particles will change until they leave the channel. As velocity increased to 10 m/d, some large agglomerates moved faster toward the outlet. The blocked area behind them grew smaller and the surface coverage increased.

The conductivity and the void fraction of the pore space are influenced by particle agglomeration. The presence of smaller and mobile agglomerates under higher flow velocities help the pore void fraction and conductivity to have large values. The conductivity is not sensitive to the flow velocity under low IS (0.001 M) conditions (Fig. 5c). However, larger agglomerates are formed under larger IS values (0.05 M or 0.3 M) and the pore conductivity becomes lower and larger variations in the local velocity field are observed. In this case, the generated force of the increased velocity remobilizes particles and agglomerates, and the pore conductivity (shown in Fig. 5c) and void fraction (Fig. 5d) can fluctuate or rise over time. Torkzaban et. al., suggested that hydrodynamic bridg-

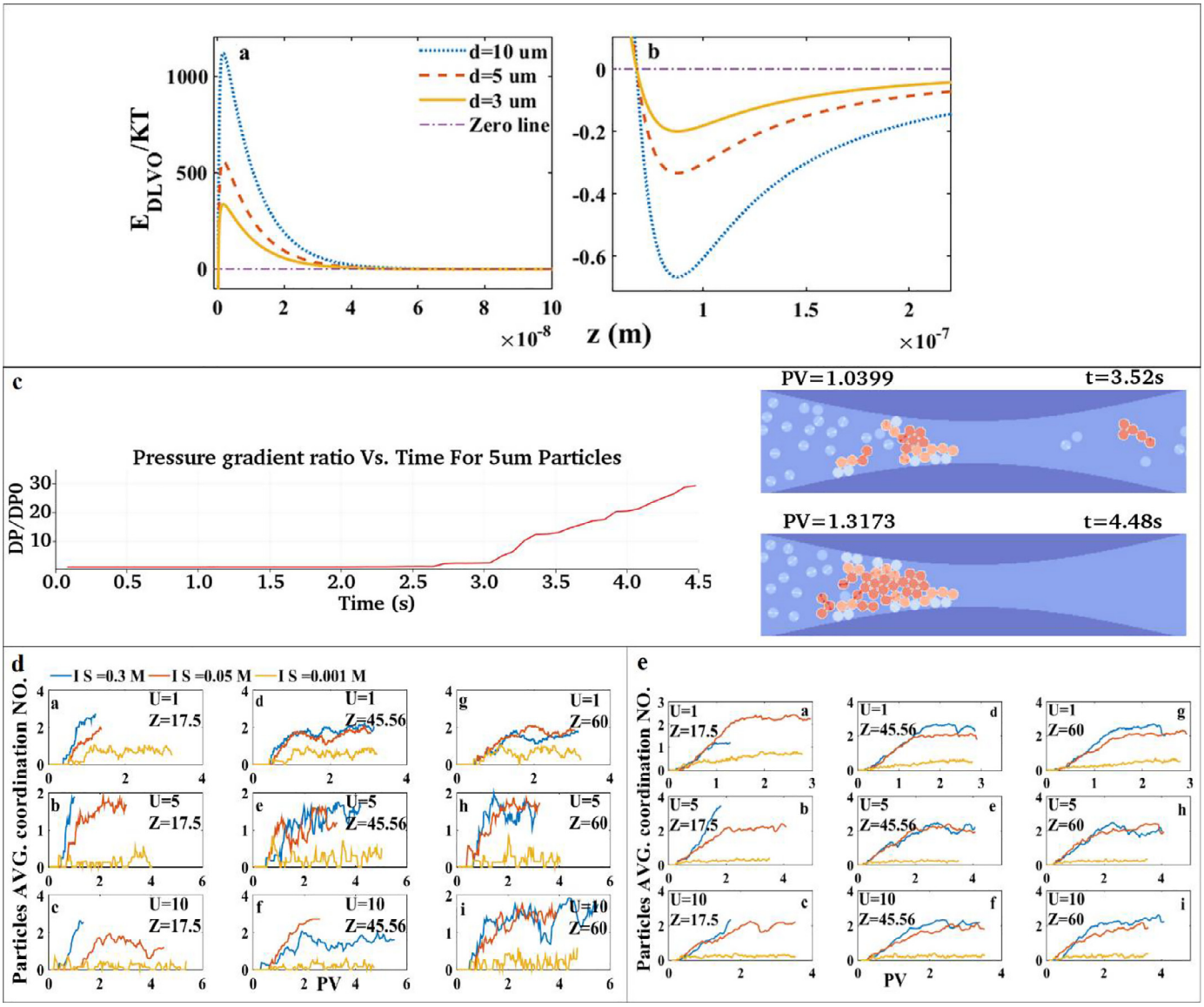

Fig. 6. Colloid size effect on particle behavior. (a, b) Development of energy barrier (plot a), and SEM region (plot b) under unfavorable conditions as d_p changes from 3 to 10 μm (IS = 0.001 M, ζ = 17.5 mV). **(c)** Strong DLVO interactions among 5 μm particles resulted in pore clogging (IS = 0.3 M, ζ = 45.56 mV, U = 5 m/d, favorable conditions). **(d, e)** Change of average coordination number of particles against injected pore volume under different IS values and unfavorable conditions: **(d)** (d_p = 10 μm). **(e)** (d_p = 3 μm). Z [mV] denotes the zeta potential and IS [M] the solution ionic strength.

ing was the main cause of permeability reductions (Torkzaban et al., 2015). They have showed that an increase in the flow velocity can break a fraction of colloid bridges and increase the permeability.

Recall that the pore conductivity was diminished as a result of clogging under favorable conditions. In contrast, unfavorable conditions were very effective in maintaining the pore conductivity due to rolling of particles over the grain surface (except for the simulations with IS = 0.3 M and ζ = 17.5 mV, shown in Fig. 5c plot g, where the combination of high IS and low zeta potential resulted in pore clogging).

Fig. 5d shows the change of pore void fraction with PV. The observed behavior corresponds with the dynamics of grain surface coverage (which is discussed before and is shown in Fig. 5b). Higher values of grain surface coverage indicate an increase in colloid retention which lowers the void fraction. Sharp reductions in the value of surface coverage corresponds with fluctuations of pore conductivity and pore void fraction (shown by the red box in plot (i) of Fig. 5b–d), and are related to previously attached large size agglomerates that move out of the pore (Fig. 5e).

4.2. Colloid size effect

Larger size colloids create stronger DLVO forces which are developed at larger distances from the grain surface and are more sensitive to IS and zeta potential changes (Fig. 6a-b). This relation makes 10 μm size colloids to be retained more easily, compared to the 5 μm or the 3 μm size colloids. Our simulations show that under favorable conditions, the 10 μm colloids clog the pore space in a short time (on the order of 1 PV), whereas the 3 μm size colloids produced much less clogging. Deposition of these large particles changes the pore structure and results in filtration of the approaching particles.

Due to stronger DLVO interactions, detachment of large size colloids and their agglomerates is unlikely unless a considerably higher flow rate is applied. Fig. 6c shows that a pore clogged with 5 μm size colloids did not able to re-open during the simulation time. The flow and chemistry conditions applied in this simulation are the same as those applied in Fig. 3d, except that a smaller colloid size of 3 μm was employed. Fig. 3d shows re-opening events for the pore due to the smaller colloid size and

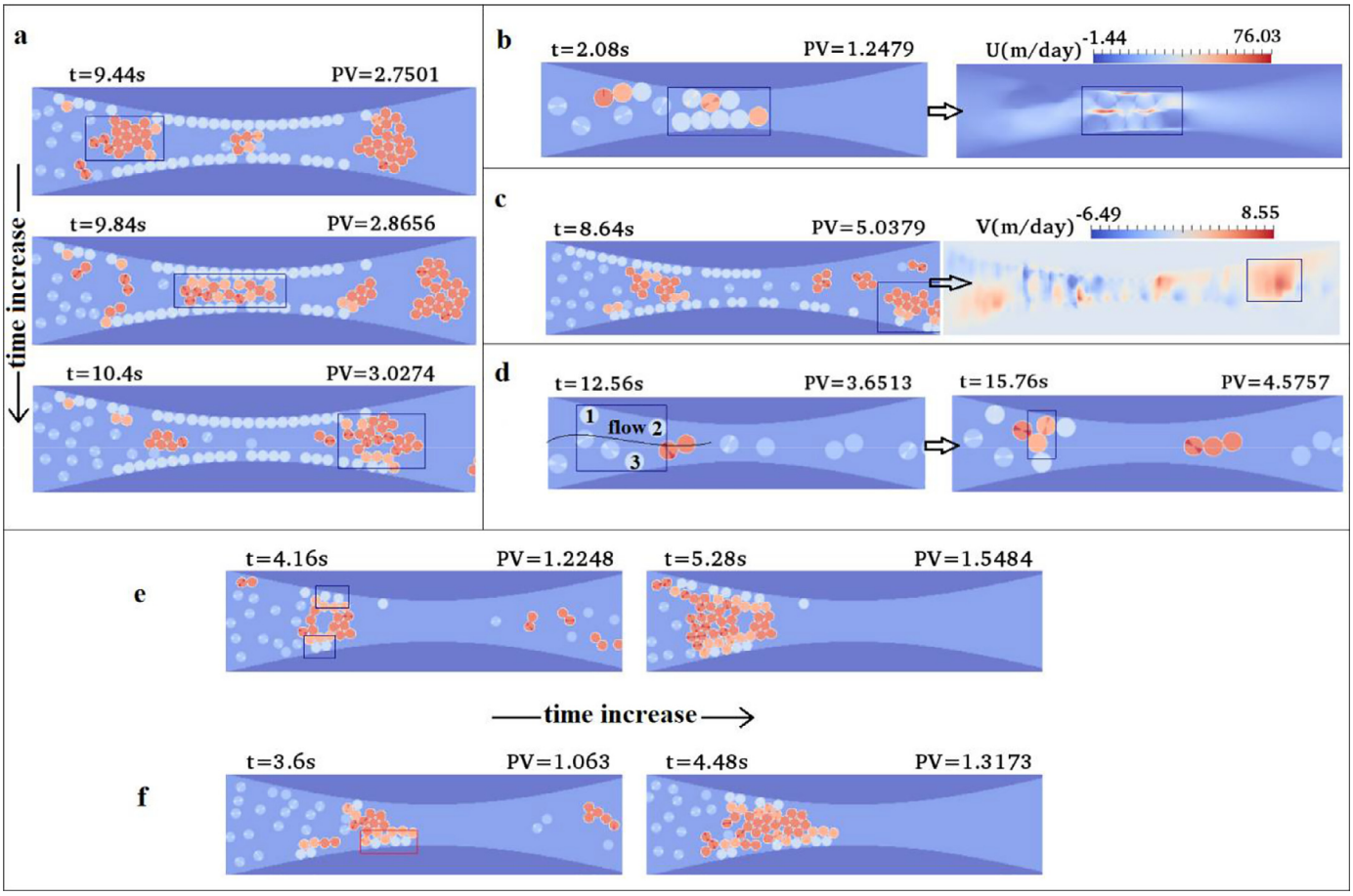

Fig. 7. Effect of pore shape on particles transport. (a) Aggregates deform and become elongated when they pass through the pore throat (d_p = 5 μm, IS = 0.05 M, ζ = 45.56 mV, U = 5 m/d, favorable conditions). **(b)** The effect of evolved pore shape on flow and velocity fields due to particles retention (d_p = 10 μm, IS = 0.05 M, ζ = 45.56 mV, U10 m/d, favorable conditions). **(c)** The deviated and accelerated flow streamlines by aggregates (d_p = 5 μm, IS = 0.05 M, ζ = 45.56 mV, U = 10 m/d, favorable conditions). **(d)** The bottleneck created by deposited particles force the approaching colloids to flow along the center of the pore where deposition is less likely to happen (d_p = 10 μm, IS = 0.001 M, ζ = 45.56 mV, U = 5 m/d, favorable conditions). **(e, f)** The location of clogging impacts the grain surface coverage that can be achieved in a pore: **(e)** (d_p = 5 μm, IS = 0.3 M, ζ = 60 mV, U = 5 m/d, favorable conditions). **(f)** (d_p = 5 μm, IS = 0.3 M, ζ = 45.56 mV, U = 5 m/d, favorable conditions).

weaker DLVO interactions. Yang and Balhoff have shown that colloid bridging becomes the controlling retention mechanism when the particle to pore size ratio is >1:7 (Yang and Balhoff, 2017).

Under unfavorable conditions the average coordination number for 10 μm particles (Fig. 6d) shows stronger fluctuations in comparison with smaller 3 μm particles (Fig. 6e) when the IS = 0.05 and 0.3 M. There are two reasons for such observations. First, the larger agglomerates need to considerably deform to pass through the narrow throat which may change the coordination number of each particle. Second, as the colloid size increases, there may be less particles available in the pore to make large agglomerates. If these agglomerates are defragmented while moving, the coordination number for a larger fraction of available particles changes and the fluctuations in agglomerates connectivity increases.

4.3. Pore structure effect

The constricted pore shape used in this study has initially converging and diverging sections to provide a non-uniform flow field. In the beginning of the simulations, the curved pore surface is also microscopically smooth (i.e., with no roughness on the curved surfaces) and chemically homogeneous. However, throughout the simulations, deposition of colloids with different sizes and charges make the pore surface increasingly heterogeneous, both physically and chemically. The evolved pore structures influence the size and form of aggregates. We have observed that generally aggregates become more elongated upon approaching the pore constriction, and afterwards then may re-form into rounded clusters (shown in Fig. 7a). The attached colloids or aggregates can significantly change the fluid streamlines. Fig. 7b shows that the 10 μm particles has squeezed the fluid into a few remaining narrow spaces where flow velocity increases. Fig. 7c shows how flow streamlines are deviated into a new path due to the presence of an agglomerate (marked in the figure using a box). As the pore space available for flow shrinks, the deviated streamlines have larger velocity magnitudes, and can mobilize colloids present in their newly-established path.

The non-uniform pore shape and particle attachments causes variable shear forces to act on particles or agglomerates in different locations of the pore space. Fig. 7d shows that the initial deposition of 10 μm particles at the pore constriction (marked by numbers 1, 2, and 3) created a partial bottleneck for other particles where the streamlines directed colloids into the center of the pore (i.e., away from the grain surface). Therefore, this simulation showed very late pore clogging in comparison with other simulations with 10 μm particles. Our simulations have shown the effect of clogging location on surface coverage. In Fig. 7e, the grain surface coverage remains lower as clogging occurs at a distance closer to the pore inlet (shown by blue boxes) in comparison with Fig. 7f.

This is because the clogging prevents accessibility of mobile colloids to downstream regions.

5. Summary and conclusions

A wide range of experimental and numerical studies have explored colloid retention and release in porous media to determine controlling mechanisms. However, there is great uncertainty in characterizing these mechanisms at the column-scale because of the complexity and coupling of many processes and factors. To overcome this limitation a model has been developed to simulate colloid transport, retention, release, and permeability alterations within a single pore. Our novel approach considers the interlink between different processes that were neglected in previous studies, including the influence of bulk and retained particles on the flow field and particle-particle interactions. The effects of hydrodynamic forces, solution IS, zeta potentials, colloid size, and pore structure on colloids transport and retention under both favorable and unfavorable conditions were subsequently investigated.

The results show that particle-particle interactions can create aggregates that rupture, deform, attach, and remobilize in the presence of various hydrodynamic forces, solution IS, and surface charge conditions. Aggregates caused complete pore clogging under favorable conditions. At the same time, attachment increased the shear force by lowering the pore space available for flow which resulted in colloid remobilizations and rupture of aggregates. The re-opening of the pore space results in sharp increases in pore hydraulic conductivity and its void fraction. Our results have shown that the flowing colloids and agglomerates can produce the required momentum to remobilize stagnant agglomerates which are often formed ahead of a pore throat where streamlines diverge, and the flow velocity decreases. Simulations under unfavorable conditions showed that the rolling of particles on the grain surface hinders pore clogging and considerably affects the shadow zone behind trapped particles. Observed differences in surface coverage and particle coordination number for favorable and unfavorable conditions were attributed to colloid rolling. When hydrodynamic forces were sufficiently strong to mobilize the agglomerates, the pore void fraction and conductivity increased, whereas the coordination number and fluid pressure gradient decreased. These findings are in agreement with previous studies based on the DLVO theory. However, our detailed direct transient simulations over a range of fluid velocities showed how the combined effects of IS, zeta potential, colloid size and pore structure alterations determine the particle deposition behavior. Moreover, we have shown and discussed how the complex and deformed flow can result in colloid transport behaviors which deviate from the expected general trends.

The observed mechanisms and their coupling provide a detail understanding that can be used to help explain and correctly model experimental observations at larger scales; e.g., breakthrough curves and retention profiles in column experiments. For example, the underlying causes for hyper-exponential and non-monotonic retention profiles and ripening processes. Furthermore, this information can be used to derive correlation equations for parameters such as retention/release rate coefficients. Insight gained from the 162 two-dimensional simulations in this work can also be used in identify specific conditions and factors that warrant additional research in 3D simulations but that are much more computationally intensive.

Author statement

All persons who meet authorship criteria are listed as authors, and all authors certify that they have participated sufficiently in the work to take public responsibility for the content, including participation in the concept, design, analysis, writing, or revision of the manuscript. Furthermore, each author certifies that this material or similar material has not been and will not be submitted to or published in any other publication before its appearance in the Journal of Petroleum Science and Engineering.

Declaration of Competing Interest

The authors declare that they have no known competing financial interests or personal relationships that could have appeared to influence the work reported in this paper.

References

Ahfir, N.D., Hammadi, A., Alem, A., Wang, H., Le Bras, G., Ouahbi, T, 2017 Mar 1. Porous media grain size distribution and hydrodynamic forces effects on transport and deposition of suspended particles. J. Environ. Sci. 53, 161–172.
Babakhani, P., 2019 Oct 1. The impact of nanoparticle aggregation on their size exclusion during transport in porous media: one-and three-dimensional modelling investigations. Sci. Rep. 9 (1), 1–2.
Bacchin, P., Derekx, Q., Veyret, D., Glucina, K., Moulin, P, 2014 Jul 1. Clogging of microporous channels networks: role of connectivity and tortuosity. Microfluid Nanofluidics 17 (1), 85–96.
Bai, R., Tien, C., 1997 Feb 15. Particle detachment in deep bed filtration. J. Colloid Interface Sci. 186 (2), 307–317.
Bakshi, S., He, Z.L., Harris, W.G, 2015 Apr 18. Natural nanoparticles: implications for environment and human health. Crit Rev. Environ. Sci. Technol. 45 (8), 861–904.
Bennacer, L., Ahfir, N.D., Alem, A., Wang, H, 2017 Jun 1. Coupled effects of ionic strength, particle size, and flow velocity on transport and deposition of suspended particles in saturated porous media. Transp. Porous Media 118 (2), 251–269.
Bouzidi, M.H., Firdaouss, M., Lallemand, P, 2001 Nov. Momentum transfer of a Boltzmann-lattice fluid with boundaries. Phys. Fluids 13 (11), 3452–3459.
Bradford, S.A., Torkzaban, S., 2013 Mar 19. Colloid interaction energies for physically and chemically heterogeneous porous media. Langmuir 29 (11), 3668–3676.
Bradford, S.A., Torkzaban, S., 2013 Mar 7. Colloid interaction energies for physically and chemically heterogeneous porous media. Langmuir 29 (11), 3668–3676.
Bradford, S.A., Yates, S.R., Bettahar, M., Simunek, J, 2002 Dec. Physical factors affecting the transport and fate of colloids in saturated porous media. Water Resour. Res. 38 (12) 63-1.
Bradford, S.A., Simunek, J., Bettahar, M., van Genuchten, M.T., Yates, S.R, 2006 Dec. Significance of straining in colloid deposition: evidence and implications. Water Resour. Res. 42 (12).
Bradford, S.A., Torkzaban, S., Walker, S.L, 2007 Jul 1. Coupling of physical and chemical mechanisms of colloid straining in saturated porous media. Water Res. 41 (13), 3012–3024.
Bradford, S.A., Kim, H.N., Haznedaroglu, B.Z., Torkzaban, S., Walker, S.L, 2009 Aug 11. Coupled factors influencing concentration-dependent colloid transport and retention in saturated porous media. Environ. Sci. Technol. 43 (18), 6996–7002.
Bradford, S.A., Torkzaban, S., Shapiro, A, 2013 Jun 11. A theoretical analysis of colloid attachment and straining in chemically heterogeneous porous media. Langmuir 29 (23), 6944–6952.
Bradford, S.A., Kim, H., Shen, C., Sasidharan, S., Shang, J, 2017 Sep 26. Contributions of nanoscale roughness to anomalous colloid retention and stability behavior. Langmuir 33 (38), 10094–11005.
Chalk, P., Gooding, N., Hutten, S., You, Z., Bedrikovetsky, P, 2012 Jan 1. Pore size distribution from challenge coreflood testing by colloidal flow. Chem. Eng. Res. Des. 90 (1), 63–77.
Chaumeil, F., Crapper, M., 2014 Aug 1. Using the DEM-CFD method to predict Brownian particle deposition in a constricted tube. Particuology 15, 94–106.
Chen, C., Waller, T., Walker, S.L, 2017. Visualization of transport and fate of nano and micro-scale particles in porous media: modeling coupled effects of ionic strength and size. Environ. Sci. 4 (5), 1025–1036.
Chrysikopoulos, C.V., Syngouna, V.I., 2014 Jun 6. Effect of gravity on colloid transport through water-saturated columns packed with glass beads: modeling and experiments. Environ. Sci. Technol. 48 (12), 6805–6813.
Das, S.K., Schechter, R.S., Sharma, M.M, 1994 Apr 1. The role of surface roughness and contact deformation on the hydrodynamic detachment of particles from surfaces. J. Colloid Interface Sci. 164 (1), 63–77.
Derjaguin, B.V., Landau, L., 1941. Theory of the stability of strongly charged lyophobic sols and of the adhesion of strongly charged particles in solutions of electrolytes. Acta Physicochim. USSR 14, 633–662.
Dunphy Guzman, K.A., Finnegan, M.P., Banfield, J.F, 2006 Dec 15. Influence of surface potential on aggregation and transport of titania nanoparticles. Environ. Sci. Technol. 40 (24), 7688–7693.
French, R.A., Jacobson, A.R., Kim, B., Isley, S.L., Penn, R.L., Baveye, P.C, 2009 Jan 21. Influence of ionic strength, pH, and cation valence on aggregation kinetics of titanium dioxide nanoparticles. Environ. Sci. Technol. 43 (5), 1354–1359.
Fujita, Y., Kobayashi, M., 2016 Jul 1. Transport of colloidal silica in unsaturated sand: effect of charging properties of sand and silica particles. Chemosphere 154, 179–186.
Gavrilescu, M., 2014 Jan 1. Colloid-mediated transport and the fate of contaminants in soils. In: In The Role of Colloidal Systems in Environmental Protection. Elsevier, pp. 397–451.
Guo, Z., Shu, C., 2013. Lattice Boltzmann Method And Its Applications in Engineering. World Scientific.
Hammadi, A., Ahfir, N.D., Alem, A., Wang, H, 2017 May 1. Effects of particle size non-uniformity on transport and retention in saturated porous media. Transp. Porous Media 118 (1), 85–98.
Henry, C., Minier, J.P, 2018 Apr 1. Colloidal particle resuspension: on the need for refined characterisation of surface roughness. J. Aerosol. Sci. 118, 1–3.

Hogg, R.T., Healy, T.W., Fuerstenau, D.W, 1966. Mutual coagulation of colloidal dispersions. Trans. Faraday Soc. 62, 1638–1651.
Hubbe, M.A., 1984 Jan 1. Theory of detachment of colloidal particles from flat surfaces exposed to flow. Colloids Surf. 12, 151–178.
Jafari, S., Yamamoto, R., Rahnama, M, 2011 Feb 9. Lattice-Boltzmann method combined with smoothed-profile method for particulate suspensions. Phys. Rev. E 83 (2), 026702.
Jin, C., Zhao, W., Normani, S.D., Zhao, P., Emelko, M.B, 2017 May 1. Synergies of media surface roughness and ionic strength on particle deposition during filtration. Water Res. 114, 286–295.
Johnson, W.P., Tong, M., 2006 Aug 15. Observed and simulated fluid drag effects on colloid deposition in the presence of an energy barrier in an impinging jet system. Environ. Sci. Technol. 40 (16), 5015–5021.
Johnson, K.L., Kendall, K., Roberts, A, 1971 Sep 8. Surface energy and the contact of elastic solids. Proc. R. Soc. London A 324 (1558), 301–313.
Katzourakis, V.E., Chrysikopoulos, C.V., 2019 Aug 1. Two-site colloid transport with reversible and irreversible attachment: analytical solutions. Adv. Water Resour. 130, 29–36.
Kim, Y.S., Whittle, A.J., 2006 Oct 1. Filtration in a porous granular medium: 1. Simulation of pore-scale particle deposition and clogging. Transp. Porous Media 65 (1), 53–87.
Ko, C.H., Elimelech, M., 2000 Sep 1. The “shadow effect” in colloid transport and deposition dynamics in granular porous media: measurements and mechanisms. Environ. Sci. Technol. 34 (17), 3681–3689.
Li, K., Ma, H., 2019 Mar 29. Rotation and retention dynamics of rod-shaped colloids with surface charge heterogeneity in sphere-in-cell porous media model. Langmuir 35 (16), 5471–5483.
Li, T., Jin, Y., Huang, Y., Li, B., Shen, C, 2017 Mar 7. Observed dependence of colloid detachment on the concentration of initially attached colloids and collector surface heterogeneity in porous media. Environ. Sci. Technol. 51 (5), 2811–2820.
Li Y., Sarishvili O., Omari A., Ahmadi A., Pu H. Colloidal particle deposition in porous media under flow: a numerical approach. 2017 Feb.
Luo, L.S., 1993. Lattice-gas automata and lattice Boltzmann equations for two-dimensional hydrodynamics. School of Physics, Georgia Institute of Technology.
McNew, C.P., Kananizadeh, N., Li, Y., LeBoeuf, E.J, 2017 Feb 1. The attachment of colloidal particles to environmentally relevant surfaces and the effect of particle shape. Chemosphere 168, 65–79.
Micić, V., Schmid, D., Bossa, N., Gondikas, A., Velimirovic, M., von der Kammer, F., Wiesner, M.R., Hofmann, T, 2017 Aug 15. Impact of sodium humate coating on collector surfaces on deposition of polymer-coated nanoiron particles. Environ. Sci. Technol. 51 (16), 9202–9209.
Morales, V.L., Zhang, W., Gao, B., Lion, L.W., Bisogni Jr, J.J., McDonough, B.A., Steenhuis, T.S, 2011 Feb 1. Impact of dissolved organic matter on colloid transport in the vadose zone: deterministic approximation of transport deposition coefficients from polymeric coating characteristics. Water Res. 45 (4), 1691–1701.
Nakayama, Y., Yamamoto, R., 2005 Mar 25. Simulation method to resolve hydrodynamic interactions in colloidal dispersions. Phys. Rev. E 71 (3), 036707.
Pelley, A.J., Tufenkji, N., 2008 May 1. Effect of particle size and natural organic matter on the migration of nano-and microscale latex particles in saturated porous media. J. Colloid Interface Sci. 321 (1), 74–83.
Perez, A.J., Patino, J.E., Soos, M., Morales, V.L, 2020 Mar 17. Morphology of shear-induced colloidal aggregates in porous media: consequences for transport, deposition and re-entrainment. Environ. Sci. Technol..
Ramachandran, V., Venkatesan, R., Tryggvason, G., Fogler, H.S, 2000 Sep 15. Low Reynolds number interactions between colloidal particles near the entrance to a cylindrical pore. J. Colloid Interface Sci. 229 (2), 311–322.
Raoof, A., Hassanizadeh, S.M., 2010. Upscaling transportof adsorbing solutes in porous media. J. Porous Media 13 (5).
Raoof, A., Hassanizadeh, S.M., Leijnse, A, 2010 Aug 1. Upscaling transport of adsorbing solutes in porous media: pore-network modeling. Vadose Zone J. 9 (3), 624–636.
Roy, S., Ghosh, S., Bhowmick, N, 2018 Jul 1. Application of colloidal filtration theory to bacterial attachment in textile fibrous media. Tekstilec 61 (3).
Saleh, N., Kim, H.J., Phenrat, T., Matyjaszewski, K., Tilton, R.D., Lowry, G.V, 2008 Apr 5. Ionic strength and composition affect the mobility of surface-modified Fe0 nanoparticles in water-saturated sand columns. Environ. Sci. Technol. 42 (9), 3349–3355.
Schijven, J.F., Hassanizadeh, S.M., 2000 Jan 1. Removal of viruses by soil passage: overview of modeling, processes, and parameters. Crit. Rev. Environ. Sci. Technol. 30 (1), 49–127.
Schijven, J.F., van den Berg, H.H., Colin, M., Dullemont, Y., Hijnen, W.A., Magic-Knezev, A., Oorthuizen, W.A., Wubbels, G, 2013 May 1. A mathematical model for removal of human pathogenic viruses and bacteria by slow sand filtration under variable operational conditions. Water Res. 47 (7), 2592–2602.
Seetha, N., Kumar, M.M., Hassanizadeh, S.M., Raoof, A, 2014 Aug 1. Virus-sized colloid transport in a single pore: model development and sensitivity analysis. J. Contam. Hydrol. 164, 163–180.
Seetha, N., Majid Hassanizadeh, S., Mohan Kumar, M.S., Raoof, A, 2015 Oct. Correlation equations for average deposition rate coefficients of nanoparticles in a cylindrical pore. Water Resour. Res. 51 (10), 8034–8059.
Sen, T.K., 2011 Mar 1. Processes in pathogenic biocolloidal contaminants transport in saturated and unsaturated porous media: a review. Water Air Soil Pollut. 216 (1–4), 239–256.
Sharma, M.M., Chamoun, H., Sarma, D.S., Schechter, R.S, 1992 Mar 1. Factors controlling the hydrodynamic detachment of particles from surfaces. J. Colloid Interface Sci. 149 (1), 121–134.
Shen, C., Lazouskaya, V., Zhang, H., Li, B., Jin, Y., Huang, Y, 2013 Sep 20. Influence of surface chemical heterogeneity on attachment and detachment of microparticles. Colloids Surf. A 433, 14–29.
Simunek, J., van Genuchten, M.T., Sejna, M, 2005 Apr 1. The HYDRUS-1D software package for simulating the one-dimensional movement of water, heat, and multiple solutes in variably-saturated media. Univ. Calif.-Riverside Res. Rep. 3, 1–240.
Succi, S., 2001 Jun 28. The Lattice Boltzmann Equation: For Fluid Dynamics and Beyond. Oxford university press.
Syngouna, V.I., Chrysikopoulos, C.V., 2012 Mar 15. Transport of biocolloids in water saturated columns packed with sand: effect of grain size and pore water velocity. J. Contam. Hydrol. 129, 11–24.
Torkzaban, S., Bradford, S.A., 2016 Jan 1. Critical role of surface roughness on colloid retention and release in porous media. Water Res. 88, 274–284.
Torkzaban, S., Bradford, S.A., van Genuchten, M.T., Walker, S.L., 2008 Feb 19. Colloid transport in unsaturated porous media: The role of water content and ionic strength on particle straining. J. Contam. Hydrol. 96 (1–4), 113–127.
Torkzaban, S., Bradford, S.A., Vanderzalm, J.L., Patterson, B.M., Harris, B., Prommer, H., 2015 Oct 1. Colloid release and clogging in porous media: Effects of solution ionic strength and flow velocity. J. Contam. Hydrol. 181, 161–171.
Torkzaban, S., Bradford, S.A., Walker, S.L, 2007 Sep 11. Resolving the coupled effects of hydrodynamics and DLVO forces on colloid attachment in porous media. Langmuir 23 (19), 9652–9660.
Verwey, E.J., Overbeek, J.T., 1948. Theory of the Stability of Lyophobic Colloids. Elsevier, Amsterdam.
Wang, C., Bobba, A.D., Attinti, R., Shen, C., Lazouskaya, V., Wang, L.P., Jin, Y, 2012 Jun 11. Retention and transport of silica nanoparticles in saturated porous media: effect of concentration and particle size. Environ. Sci. Technol. 46 (13), 7151–7158.
Xinqiang, D., Yalin, S., Xueyan, Y., Ran, L, 2019 Feb 28. Colloid clogging of saturated porous media under varying ionic strength and roughness during managed aquifer recharge. J. Water Reuse Desalin..
Yang, H., Balhoff, M.T., 2017 Jul. Pore-network modeling of particle retention in porous media. AIChE J. 63 (7), 3118–3131.
Yao, K.M., Habibian, M.T., O’Melia, C.R, 1971 Nov 1. Water and waste water filtration. Concepts and applications. Environ. Sci. Technol. 5 (11), 1105–1112.
Zevi, Y., Dathe, A., Gao, B., Zhang, W., Richards, B.K., Steenhuis, T.S, 2009 Dec 1. Transport and retention of colloidal particles in partially saturated porous media: effect of ionic strength. Water Resour. Res. 45 (12).
Zhang, W., Niu, J., Morales, V.L., Chen, X., Hay, A.G., Lehmann, J., Steenhuis, T.S, 2010 Dec. Transport and retention of biochar particles in porous media: effect of pH, ionic strength, and particle size. Ecohydrology 3 (4), 497–508.
Zhang, Q., Raoof, A., Hassanizadeh, S.M, 2015. Pore-scale study of flow rate on colloid attachment and remobilization in a saturated micromodel. J. Environ. Qual. 44 (5), 1376–1383.
Zhang, C., Yan, A., Wang, G., Jin, C., Chen, Y., Shen, C, 2018 May 1. Impact of flow velocity on transport of graphene oxide nanoparticles in saturated porous media. Vadose Zone J. 17 (1).
Messina, F., Sethi, R., Marchisio, D, 2015 April. Pore-scale simulation of micro and nanoparticle transport in porous media (PhD Dissertation). Politecnico di Torino Porto Institutional Repository.